Pitting corrosion behaviour in sodium chloride solution of intermetallic centreline stringers in super duplex stainless steels

P. Erazmus-Vignal, V. Vignal, P. Huguenin, F. Krajcarz

Pitting corrosion behaviour in sodium chloride solution of intermetallic centreline stringers in super duplex stainless steels

P. Erazmus-Vignal[a], V. Vignal[b,1], P. Huguenin[c], F. Krajcarz[c]

[a] *SATT SAYENS, 64 A rue de Sully, CS 77124, 21071 Dijon Cedex, France*

[b] *ICB, UMR 6303 CNRS - Université de Bourgogne Franche Comté, BP 47870, 21078 Dijon Cedex, France*

[c] *APERAM R&D – BP 15, rue Roger Salengro, 62330 Isbergues, France*

ABSTRACT

Although manufacturers have optimized metallurgical routes to deliver super duplex stainless steels free from intermetallic phases, a segregated zone is generally formed close to mid-thickness for flat products. This zone may contain a small amount of sigma phase particles in the form of centerline intermetallic stringers. In this paper, their corrosion behaviour is investigated in sodium chloride solution, by coupling non-electrochemical and electrochemical techniques at the global and local scales. Corrosion mechanisms at centerline intermetallic stringers is then discussed and weak points in the sample are identified.

Key-words: super duplex stainless steels, corrosion, sigma phase

[1] Corresponding author : Vincent Vignal : email: Vincent.vignal@u-bourgogne.fr

1. Introduction

Super duplex stainless steels (SDSS) are used in many industrial sectors (such as marine environment, petrochemical, oil and gas, chemical and desalination industries), requiring materials with superior corrosion and mechanical properties. Due to their high chromium and molybdenum content, SDSS grades are known to be more sensitive to intermetallic phase precipitation (sigma phase, for example) than other grades [1-3].

Therefore, manufacturers have optimized metallurgical routes to deliver SDSS products free from intermetallic phases. However, during solidification, conventional casting processes may induce a slight local modification of the chemical composition by solute partitioning. Segregated zones containing higher concentration of both austenite-formers (Ni and N) and ferrite-formers (Cr and Mo) are generally formed close to mid-thickness for flat products. Further thermal-mechanical treatments such as hot-rolling, annealing and cold-rolling tend to flatten and stretch the segregations zones, while limiting the segregation rate by solid diffusion of solute toward the surrounding material. These zones are more susceptible to intermetallic phase precipitation, such as σ-phase. According to the international standard ISO 17781 [4], the centerline intermetallic stringers are then defined as a group of intermetallic phases (sigma, χ-phase and R-phase) aligned within the mid-thickness area due to alloy segregation.

There is no study of the corrosion behavior of centerline intermetallic stringers in duplex stainless steels. A paper deals with the influence of centerline intermetallic stringers on the susceptibility to hydrogen induced stress cracking of UNS S32750 [5]. It was shown that intermetallic phases in centerline stringers have negligible influence on the hydrogen embrittlement susceptibility of SDDS.

By contrast, many papers concern the influence of sigma phase on the corrosion resistance of duplex stainless steels [6-17]. In these papers, sigma was formed by heat treatment in Laboratory furnace under different experimental conditions (to control the volume fraction, size

and shape,…). Sigma was also formed during welding [7]. The general trend of all published results is that the presence of sigma in the alloy results in the deterioration of its corrosion resistance. This was observed in various aqueous media (acidic solutions, artificial sea water…).

It was reported [6-17] that secondary austenite and other precipitates (such as χ phase, nitrides and carbides) may also be formed in Laboratory furnace. It is then difficult to deconvolute the role of sigma in the overall response derived from classical techniques at the global scale, which also depends on the presence of other precipitates. In addition, the microstructures obtained under Laboratory conditions are different from that generated during conventional casting processes. Extrapolating data obtained under Laboratory conditions on centerline intermetallic stringers is a complicated task.

In the present paper, the microstructure of UNS S32750 SDSS is first investigated using field emission scanning electron microscopy equipped with energy dispersive X-ray spectroscopy (FE-SEM/EDS) and field emission transmission electron microscopy coupled with EDS (FE-TEM/EDS). Particular attention is paid to the centerline intermetallic stringers. The corrosion behavior of this alloy is then studied using potentiodynamic measurements at the local and global scales and the potentiostatic pulse testing (PPT) method. These experiments were combined with surface observations (FE-SEM/EDS and atomic force microscopy (AFM)). The influence of the microstructure (especially the presence of sigma) on the corrosion resistance is analysed and discussed.

2. Materials and methods

2.1. Specimens and surface preparation

Experiments were performed on UNS S32750 SDSS (chemical composition: C: 0.017 wt.%, N: 0.27 wt%, Cr: 26 wt%, Mn: 0.9 wt%, Mo: 3.8 wt.%, Ni: 7 wt%, Si: 0.3 wt%, and Fe: bal.).

Samples were extracted from a plate (thickness of 6 mm), cut from a coil made from continuously-casted slab which was then hot-rolled, solution annealed & pickled. As centerline intermetallic stringers are rare and randomly distributed in the plate, preliminary extensive sampling coupled with light optical microscopy (LOM) after NaOH electroetching was performed to select samples containing centerline intermetallic stringers close to mid-thickness. The volume fraction of ferrite in the bulk alloy is 52.6% and the austenite spacing is 3.4±0.5 μm. The austenite spacing is defined as the average distance in the ferrite between austenite grains.

Samples were cut from plates using a diamond band saw and embedded in an epoxy resin. The cross-sectional surface (surface area of 25 ×5 mm^2) corresponding to the longitudinal surface normal to the long-transverse direction of the plate was then ground using emery papers (down to 4000 grade) and polished with diamond pastes (down to 1 μm). Between each step, samples were cleaned in ethanol under ultrasonics for 3 minutes. After polishing, the segregated zone (SZ) and the sigma phase are visible in the middle of the plate, Fig. 1(a).

2.2. Electrochemical measurements

UNS S32750 SDSS is selected by users for its good corrosion resistance in chloride environments such as those found in oil & gas and marine applications. All electrochemical tests were carried out in 3M NaCl, pH =1 (acidified with H_2SO_4) at 80 °C using a PGSTAT128 AUTOLAB potentiostat/galvanostat. These very aggressive conditions were defined during a preliminary work (not shown here) to have successively the presence of a passive range and stable pitting corrosion in the anodic domain.

Global and local polarization curves were plotted at a potential scan rate of 1 mV/s and from an applied potential of -0.5 V vs. Ag/AgCl (reference electrode). The preliminary work also showed that no additional information is derived from polarization curves plotted by applying lower potential scan rates (0.1 and 0.5 mV/s). The counter electrode was made of platinum. No prior polarisation in the cathodic domain was applied to the system. Global polarization curves were plotted using a classical three-electrode cell. On the other hand, local polarization curves were determined using the electrochemical microcell technique [18-20] with a capillary diameter of 45 μm. A description of this technique is provided in [21]. As the measured current was extremely low, the electrochemical microcell was placed in a Faraday cage. Samples were heated using a Peltier heating stage (Linkam 190). This stage was electrically insulated from the sample and connected to the ground.

By contrast to potentiodynamic experiments, the potentiostatic pulse testing (PPT) permits to control the size and density of micro-pits. PPT consists in applying a potential E_A (0.3 and 1 V vs. saturated calomel electrode (SCE, reference electrode)) for 1 second and then a potential of –0.5 V vs. SCE in the cathodic domain (passive behaviour) for 1 second. This procedure was repeated N cycles (N = 10, 20 or 30). The values of the number of cycles were defined during the preliminary work (not shown here) to be able to identify the different steps of dissolution. The counter electrode was made of platinum disk (diameter of 1 cm). After PPT tests, the specimen surface was cleaned in ethanol under ultrasonics and then observed by FE-SEM/EDS and AFM.

The occurrence of crevice corrosion during electrochemical tests was prevented by sealing the interface between the polished specimen and epoxy resin with an acrylic coating (M-coat D from Vishay). The acrylic coating was dried in air at 25°C for 12 hours. After electrochemical tests, the interface between the specimen and epoxy resin was observed to confirm that no crevice was formed.

2.3. Surface observations

A field-emission type scanning electron microscope (JEOL 7600F) with an integrated electron dispersion spectrometer (FE-SEM/EDS) was used to determine the morphology and the chemical composition of phases at the microscale. Images were acquired in the low-angle back scattered electron (LABE) mode at an accelerating voltage of 15 kV. This detector is capable of producing qualitative compositional images with a very high degree of atomic number contrast. Images were also acquired in lower secondary electron imaging (LEI) mode at 15 kV to have topographical information.

Field-emission type transmission electron microscopy (FE-TEM) studies at the nanoscale were carried out using a JEOL JEM-2100 microscope with a LaB6 source operating at 200 kV. Regarding chemical analysis, EDS spectra were acquired on a JED-2300T coupled to the FE-TEM microscope. In terms of sample preparation, classical grinding, polishing and dimpling methods (Dimple Grinder Model 656 from Gatan) followed by ion beam milling (PIPS Model 691 from Gatan) were used to obtain a sample thickness that would be transparent to high energy electrons.

3D images of the specimen surface were obtained from atomic force microscopy (AFM, Q-Scope 350 from Quesant Instrument Corporation). AFM Images were acquired in tapping mode (vibration frequency: 174 kHz) and they were analyzed using the Q-analysis 4.0 software package.

3. Results and discussion

3.1. Microstructure

Fig. 1(a) shows the presence of clustered precipitates (also called stringers) in the UNS S32750 SDSS derived from conventional casting processes. These precipitates appear in white

color in FE-SEM images. They are likely aligned along the rolling direction and grow in a discontinuous segregated zone located close to the middle of the plate (centerline intermetallic stringers). These precipitates vary in size and distribution depending on the magnitude of the compositional segregation. FE-SEM/EDS analyses show that austenite and ferrite in the segregated zone are richer in chromium and molybdenum than the matrix far from it, Table 1. The pitting resistance equivalent number (PREN) of both phases in the SZ was then found to be greater than that of phases outside the SZ (difference of 4.5 and 7 for the austenite and ferrite, respectively). This increase of PREN in the SZ has significant effect on its corrosion resistance. For example, an increase of PREN of 5 units leads to an increase of the critical pitting temperature of DSS immersed in sea water of approximately 20°C [22].

FE-SEM/EDS analyses show that particles contain 30 wt.% of chromium and 8.1 wt.% of molybdenum (statistical data on numerous precipitates, Table 1). This result indicate that they are richer in chromium and molybdenum than the surrounding matrix located in the segregated zone (Table 1). In addition, several particles and the surrounding matrix were examined by means of selected area electron diffraction (SAED) measurements using FE-TEM. Fig. 2(a-d) shows an investigated particle and the corresponding SAED patterns. The patterns of ferrite (Fig. 2(b)) and austenite (Fig. 2(c)) grains were indexed considering the body centered cubic (space group 1-3m) and face centered cubic (space group Fm-3m) systems, respectively. The pattern of the particle was successfully indexed considering the tetragonal system (space group P42/mnm), Fig. 2(d). FE-TEM/EDS analyses were performed in the three sites (points 1-3 in Fig. 2(a)). Results are reported in Table 2. They confirm that the particle is enriched in Mo and Cr with respect to the matrix. Therefore, the results presented above indicate that clustered precipitates are sigma phase which is a chromium/molybdenum-rich intermetallic phase [23] crystallizing in the tetragonal system [24].

It is known that the decomposition of ferrite can lead to the formation of sigma phase and secondary austenite γ_2 [25-28]. It was shown that secondary austenite contains less chromium and molybdenum than primary austenite [29-30], and therefore has a lower PREN value than primary austenite [7]. Fig. 1(b) shows the presence of another phase in the sigma particles, probably secondary austenite. FE-TEM/EDS measurements performed on several grains of this phase give (wt.%): 25.2±0.5% Cr, 1.3±0.3% Mn, 6.7±0.5wt.% Ni, 1±0.2wt.% Mo and 65.8±0.5wt.% Fe. This phase is poorer in chromium (ΔCr = -2.5 wt.%), molybdenum (ΔMo = -3 wt.%) and nickel (ΔNi = -4 wt.%) compared to the primary austenite present in the SZ. This result is in good agreement with those of the literature, confirming that secondary austenite is formed.

A depleted zone is only observed at the interface between sigma precipitates and ferrite grains. The depletion in chromium at this location is of about 10 wt.% (Fig. 3(a)). The depleted zone extends over a distance of about 200 nm. No depleted zone is detected by means of FE-TEM/EDS at the interface between primary austenite grains and sigma precipitates and between secondary austenite grains and sigma precipitates, Fig. 3(b). No other segregation is observed at the austenite / sigma interface (such as carbides, nitrides and χ phase). Therefore, the microstructure described here is very different from that studied in the literature. In this previous case [6-17], sigma phase is present throughout the volume of the alloy, segregation of different particles occurs (nitrides, carbides, χ phase), a chromium-depleted zone can exist at the austenite/sigma interface, and there is no segregated zone.

3.2. Corrosion behavior of the alloy at the global scale

Fig. 4(a) shows the global polarization curve of the alloy in 3M NaCl (pH=1) at 80°C. As explained in section 2.1, this curve was plotted on the cross-sectional surface (that contains the SZ), after polishing. A small current peak is first observed in the anodic domain (graph insert

in Fig. 4(a)), followed by a narrow passive range (between -0.33 and 0 V vs Ag/AgCl). This passive range is associated with a current density of about 13 $\mu A/cm^2$.

Surface observations were performed by means of FE-SEM after interrupting the polarization curve at -0.2 V vs Ag/AgCl corresponding to the end of the current peak. The interface between ferrite grains and sigma particles (where the chromium depleted zone was observed by means of FE-TEM/EDS) is dissolved, Fig. 5(a-b). This leads to the formation of shallow trenches. These trenches are visible at the interface between sigma and ferrite grains on AFM images, Fig. 5(c). By contrast, the interface between austenite grains and sigma (where there is no chromium depleted zone) is intact. No trenches are observed at these locations by means of FE-SEM and AFM (Fig. 5(c)). Therefore, the current peak is first related to the dissolution of the chromium depleted zone at the interface between sigma precipitates and ferrite grains. The current peak is also related to the uniform dissolution of the secondary austenite (Fig. 6(a-c)). The different phases present in Fig. 6(a-c) were identified from FE-SEM/EDS analyses (Table 3). The dissolution of the secondary austenite was revealed by AFM observations (Fig. 6(d)). However, no pits are observed (only trenches at the interfaces and cavities where secondary austenite was located). Within this potential range, sigma precipitates remain intact (no dissolution).

Stable pitting occurs from an applied potential of 0 V vs Ag/AgCl (Fig. 4(a)). Surface observations by means of FE-SEM performed after the global polarization curve reveal the existence of two pits (Fig. 4(b-c)). Both initiated at oxide particles located in the matrix, at a distance of between 600 and 900 µm from the segregated zone. These particles can be considered as the weakest sites in the sample. They are composed of aluminum, magnesium and calcium oxides. FE-SEM/EDS analysis of the particle visible in Fig. 4(c) yields 48.5 wt.% O, 15.8wt.% Mg, 34.2wt.% Al and 1.2 wt.% Ca. It was already shown that pits initiate preferentially at oxide particles in duplex stainless steels [10, 31], austenitic stainless steels [32]

and pipeline steels [33]. No changes in the segregated zone compared to those observed after the current peak were noted beyond the pitting potential (Fig. 4(d)). This means that under the selected experimental conditions the segregated zone is not a precursor site for pitting. The rapid current density increase observed beyond the pitting potential is only due to the pits observed far from the segregated zone.

3.3. Corrosion behavior of the stringers

The corrosion behavior of stringers cannot be studied using classical techniques at the global scale because pitting is initiated for relatively low potential values at oxide particles (the stringers remaining passive). Therefore, to identify corrosion mechanisms of stringers both local electrochemical experiments and PPT tests were carried out.

Local polarization curves were plotted using the electrochemical microcell technique (microcapillary diameter of 45 µm). No oxide particles (where stable pitting is observed at the global scale, grey curve in Fig. 4(a)) were present under the microcapillary. Local experiments were first conducted in the matrix of the segregated zone free of sigma (red curves in Fig. 4(a)) and in the matrix far from the segregated zone (blue curves in Fig. 4(a)). Local experiments in both types of sites were repeated several times to check the reproducibility of the results.

Although they do not have the same composition (Table 1), these two types of sites exhibit very similar corrosion behavior. The corrosion potential is around -0.3 V vs Ag/AgCl. Above 0.85 V vs Ag/AgCl, the current density increases sharply, in relation with the water dissociation reaction (Reaction 1). FE-SEM observations of the two surfaces after the test show that no pits initiated. Therefore, both sites exhibit a large passive range. The only noticeable difference is the value of the current density in the passive range. It is around 9 and 15 $\mu A/cm^2$ for the matrix in the segregated zone and the matrix far from the segregated zone, respectively. These values were measured in the middle of the current plateau (at + 0.2 V vs Ag/AgCl) of polarization

curves. The decrease of the current density observed in the SZ may be due to the fact that its PREN is significantly greater than that of the matrix outside the SZ (see section 3.1).

$$2H_2O \rightarrow 4e^- + 4H^+ + O_2 \quad (1)$$

In the presence of sigma precipitates under the microcapillary, stable pitting was detected at roughly 0.85 V vs Ag/AgCl (black curves in Fig. 4(a)). FE-SEM observations of these sites after the test show the existence of pits (Fig. 4(e)). Therefore, sites containing sigma precipitates can be sensitive to pitting corrosion, but only at very high values of the applied potential. The nature of the weak point in these sites could not be identified using the electrochemical microcell technique.

To determine the nature of these weak points and the role of sigma precipitates, a series of PPT experiments were carried out followed by FE-SEM/EDS observations. The choice of experimental conditions for these PPT tests was performed considering the results derived from global and local polarization curves. Experiments were first performed at E_A= 0.3 V vs SCE. This value is beyond the pitting potential of oxide particles (grey curve in Fig. 4(a)), but below the pitting potential of the matrix in the segregated zone (black curve in Fig. 4(a)). The same results were obtained for 10 and 30 cycles (Fig. 7(a)-(b)). Secondary austenite and the chromium depleted zone at the sigma/ferrite interface are dissolved (confirmed by AFM observations). The dissolution of these two types of zones does not lead to the propagation of pits in the matrix in the close vicinity of sigma. However, as it was shown previously (Fig. 4(b-c)), some pits initiate at oxide particles outside the segregated zone. This is in good agreement with the experiments conducted at the global scale showing that the segregated zone remains passive within this potential range.

PPT tests with an applied potential E_A equal to 0.85 V vs SCE (and N = 10, 20 cycles) lead to the same conclusions as previously (dissolution of secondary austenite and the chromium

depleted zone and no dissolution of sigma and matrix). This value of E_A is located at the end of the passive range.

The value of E_A was then set at 1 V vs SCE (N = 10 cycles). This value is beyond the pitting potential of the matrix in the segregated zone (of about 0.85 V vs Ag/AgCl, black curve in Fig. 4(a)). Under these conditions, secondary austenite and the chromium depleted zone are again preferentially dissolved (Fig. 7(c)). By contrast to the two previous cases (0.3 and 0.85 V vs SCE), pits propagate in the ferrite from the crevices formed by the dissolution of the chromium depleted zone (Fig. 7(c)). With increasing number of cycles (N=20 cycles), pits continue to grow and large pits are found (Fig. 7(d). Sigma precipitates, which are passive up to E_A=0.85 V vs SCE, start to dissolve (Fig. 7(e)). Transpassive dissolution of pure chromium [24] and chromium containing alloys [35-41] was already observed and studied. It was demonstrated that these alloys are susceptible to transpassive dissolution because the oxides formed at their surface are not stable at high applied potentials [40]. In addition, the current density in the transpassive domain (and therefore the corrosion rate) increases with increasing chromium content in the alloy [41]. Dissolution of sigma was confirmed by AFM observations (Fig. 8(a-b). These surface observations show that dissolution of sigma occurs preferentially in the vicinity of secondary austenite (red circle in Fig. 8(b)). This may be due to a crevice effect after dissolution of γ_2 at lower potentials).

4. Conclusions

The corrosion behaviour of centerline intermetallic stringers (UNS S32750 SDSS) was investigated in the following aggressive conditions: 3M NaCl (pH =1) at 80 °C, by coupling non-electrochemical and electrochemical techniques at the global and local scales. The following conclusions can be drawn:

1) Sigma exists in the form of clustered precipitates oriented along the rolling direction. They are observed in a segregated zone located in the middle of the plates. This segregated zone has a greater PREN value than the matrix outside it (difference of about 6). Sigma precipitation is known to induce the formation of secondary austenite.

2) The weakest sites of the alloy contain oxide inclusions (pitting potential around 0 V vs Ag/AgCl) and are not centreline intermetallic stringers.

3) Within a wide potential range in the anodic domain (below 0.85 V vs SCE), secondary austenite and the chromium depleted zone at the ferrite/sigma interfaces dissolve, but no pits are observed. Sigma remains intact.

4) Sites containing sigma precipitates are sensitive to pitting corrosion only at very high values of the applied potential (above 0.85 V vs SCE). Pits were found to propagate in the ferrite, from crevices formed during the dissolution of γ_2 and the chromium depleted zone. At the onset of this step, sigma remains intact. With increasing number of cycles during PPT, sigma starts to undergo transpassive dissolution. It occurs locally, in the vicinity of γ_2 where the chromium content is very high.

Stringers are formed in a segregated zone whose PREN is significantly higher than that of the matrix outside of it. The difference of PREN is high enough (in the order of 5) to assume that the corrosion resistance of the segregated zone is significantly higher than that of the matrix outside of it (which is equivalent to the matrix considered in the studies already published in the literature). Therefore, by contrast to the results published in the literature on sigma phase having precipitated after prolonged time in the sigma phase stability temperature range (or after unsufficient cooling), discontinuous centerline intermetallic stringers, as described in the current paper, do not impair the overall pitting corrosion resistance of the alloy.

References

[1] C.C. Hsieh, W. Wu, Overview of intermetallic sigma (σ) phase precipitation in stainless steels, ISRN Metallurgy (2012), 732471, https://doi.org/10.5402/2012/732471.

[2] D.M.E. Villanueva, F.C.P. Junior, R.L. Plaut, A.F. Padilha, Comparative study on sigma phase precipitation of three types of stainless steels: austenitic, superferritic and duplex, J. Mater. Sci. Technol. 22 (2006) 1098-1104, https://doi.org/10.1179/174328406X109230.

[3] R. Wang, Precipitation of sigma phase in duplex stainless steel and recent development on its detection by electrochemical potentiokinetic reactivation: a review, Corros. Comm. 2 (2021) 41-54, https://doi.org/10.1016/j.corcom.2021.08.001.

[4] International standard ISO 17781:2017, Petroleum, petrochemical and natural gas industries — Test methods for quality control of microstructure of ferritic/austenitic (duplex) stainless steels.

[5] F. Krajcarz, F. Ruel, S. Saedlou, Effect of the superduplex microstructure on the susceptibility to hydrogen induced stress cracking, Paper presented at the CORROSION 2019, Paper Number: NACE-2019-13062, Nashville, Tennessee, USA, March 2019.

[6] M.E. Wilms, V.J. Gadgil, J.M. Krougman, F.P. Ijsseling, The effect of σ-phase precipitation at 800 °C on the corrosion resistance in sea-water of a high alloyed duplex stainless steel, Corros. Sci. 36 (1994) 871-881, https://doi.org/10.1016/0010-938X(94)90176-7.

[7] Z. Zhang, H. Jing, L. Xu, Y. Han, L. Zhao, The influence of microstructural evolution on selective corrosion in duplex stainless steel flux-cored arc welded joints, Corros. Sci. 120 (2017) 194-210, https://doi.org/10.1016/j.corsci.2016.12.007.

[8] D. Zou, Y. Han, W. Zhang, G.W. Fan, Phase transformation and its effects on mechanical properties and pitting corrosion resistance of 2205 duplex stainless steel, J. Iron teel Res. Int. 17 (2010) 67-72, https://doi.org/10.1016/S1006-706X(10)60172-0.

[9] B. Deng, Z. Wang, Y. Jiang, H. Wang, J. Gao, J. Li, Evaluation of localized corrosion in duplex stainless steel aged at 850 °C with critical pitting temperature measurement, Electrochim. Acta 54 (2009) 2790–2794, https://doi.org/10.1016/j.electacta.2008.11.038.

[10] J. Gao, Y. Jiang, B. Deng, Z. Ge, J. Li, Determination of pitting initiation of duplex stainless steel using potentiostatic pulse technique, Electrochim. Acta 55 (2010) 4837–4844, https://doi.org/10.1016/j.electacta.2010.02.035.

[11] H. Zhao, Z. Zhang, H. Zhang, J. Hu, J. Li, Effect of aging time on intergranular corrosion behavior of a newly developed LDX 2404 lean duplex stainless steel, J. Alloys and Compd. 672 (2016) 147-154, https://doi.org/10.1016/j.jallcom.2016.02.101.

[12] Y.H. Yang, B. Yan, J. Wang, J.L. Yin, The influence of solution treatment temperature on microstructure and corrosion behavior of high temperature ageing in 25% Cr duplex stainless steel, J. Alloys and Compd. 509 (2011) 8870-8879, https://doi.org/10.1016/j.jallcom.2011.06.099.

[13] A. Moteshakker, I. Danaee, Microstructure and Corrosion Resistance of Dissimilar Weld-Joints between Duplex Stainless Steel 2205 and Austenitic Stainless Steel 316L, J. Mater. Sci. Technol. 32 (2016) 282-290, https://doi.org/10.1016/j.jmst.2015.11.021.

[14] V.S. Moura, L.D. Lima, J.M. Pardal, A.Y. Kina, R.R.A. Corte, S.S.M. Tavares, Influence of microstructure on the corrosion resistance of the duplex stainless steel UNS S31803, Mater. Charact. 59 (2008) 1127- 1132, https://doi.org/10.1016/j.matchar.2007.09.002.

[15] R.A. Perren, T. Suter, C. Solenthaler, G. Gullo, P.J. Uggowitzer, H. Bohni, M.O. Speidel, Corrosion resistance of super duplex stainless steels in chloride ion containing environments: investigations by means of a new microelectrochemical method II. Influence of precipitates, Corros. Sci. 43 (2001) 727-745, https://doi.org/10.1016/S0010-938X(00)00088-3.

[16] E. Angelini, B. De Benedetti, F. Rosalbino, Microstructural evolution and localized corrosion resistance of an aged superduplex stainless steel, Corros. Sci. 46 (2004) 1351–1367, https://doi.org/10.1016/j.corsci.2003.09.024.

[17] M. Martinsa, L.C. Casteletti, Microstructural characteristics and corrosion behavior of a super duplex stainless steel casting, Mater. Charact. 60 (2009) 150-155, https://doi.org/10.1016/j.matchar.2008.12.010.

[18] H. Krawiec, V. Vignal, J. Banas, Local electrochemical impedance measurements on inclusion-containing stainless steels using microcapillary-based techniques, Electrochim. Acta 54 (2009) 6070-6074, https://doi.org/10.1016/j.electacta.2008.12.022.

[19] H. Krawiec, Z. Szklarz, Combining the Electrochemical Microcell Technique and the Electron Backscatter Diffraction method to study the electrochemical behaviour of polycrystalline aluminium in sodium chloride solution, Electrochim. Acta 203 (2016) 426-438, https://doi.org/10.1016/j.electacta.2016.03.030.

[20] J. Gravier, V. Vignal, S. Bissey-Breton, Influence of residual stress, surface roughness and crystallographic texture induced by machining on the corrosion behaviour of copper in salt-fog atmosphere, Corros. Sci. 61 (2012) 162-170, https://doi.org/10.1016/j.corsci.2012.04.032.

[21] H. Krawiec, V. Vignal, R. Akid, Numerical modelling of the electrochemical behaviour of 316L stainless steel based upon static and dynamic experimental microcapillary-based techniques, Electrochim. Acta 53 (2008) 5252-5259, https://doi.org/10.1016/j.electacta.2008.02.063.

[22] In Duplex stainless steels: Microstructure, Properties and Applications, Third Edition, Editor : R. Gunn, Woodhead Publishing Ltd (UK), Chapter 6 (2003) 71-91.

[23] G.S. da Fonseca, P.S.N. Mendes, A.C.M. Silva, Sigma Phase: Nucleation and Growth, Metals, 9 (2019) 34, https://doi.org/10.3390/met9010034.

[24] C.-C. Hsieh, W. Wu, Overview of Intermetallic Sigma (σ) Phase Precipitation in Stainless Steels, Int. Sch. Res. Notices, (2012) 732471, https://doi.org/10.5402/2012/732471.

[25] D.E. Villanueva, F. Junior, R. Plaut, A. Padilha, Comparative study on sigma phase precipitation of three types of stainless steels: austenitic, superferritic and duplex, Mater. Sci. Technol. 22 (2006) 1098–1104, https://doi.org/10.1179/174328406X109230.

[26] A. Padilha, D. Escriba, E. Materna-Morris, M. Rieth, M. Klimenkov, Precipitation in AISI 316L (N) during creep tests at 550 and 600 C up to 10 years, J. Nucl. Mater. 362 (2007) 132–138, https://doi.org/10.1016/j.jnucmat.2006.12.027.

[27] D.Y. Kobayashi, S. Wolynec, Evaluation of the low corrosion resistant phase formed during the sigma phase precipitation in duplex stainless steels, Mater. Res. 2 (1999) 239–247, https://doi.org/10.1590/S1516-14391999000400002.

[28] A. D. Warren, R.L. Harniman, Z. Guo, C. M. Younes, P. E. J. Flewitt, T. B. Scott, Quantification of sigma-phase evolution in thermally aged 2205 duplex stainless steel, J Mater Sci 51 (2016) 694–707, https://doi.org/10.1007/s10853-015-9131-9.

[29] J.-O. Nilsson, L. Karlsson, J.-O. Andersson, Secondary austenite formation and its relation to pitting corrosion in duplex stainless steel weld metal, Mater. Sci. Technol., 11 (1995) 276-283, https://doi.org/10.1179/mst.1995.11.3.276.

[30] T. Kuroda, F. Matsuda, Role of Secondary Austenite on Corrosion and Stress Corrosion Cracking of Sensitized Duplex Stainless Steel Weldments, 23 (1994) 205-211, https://doi.org/10.18910/12721.

[31] V. Vignal, N. Mary, R. Oltra, J. Peultier, Mechanical–electrochemical approach for the determination of precursor sites for pitting corrosion at the microscale, J. Electrochem. Soc. 153, (2006), B352-B357, https://doi.org/10.1149/1.2218762.

[32] N. Hara, K. Hirabayashi, Y. Sugawara & I. Muto, Improvement of pitting corrosion resistance of type 316L stainless steel by potentiostatic removal of surface MnS inclusions, Int. J. Corros. 2012, (2012), 482730, https://doi.org/10.1155/2012/482730.

[33] Z. Yang, B. Kan, J. Li, Y. Su, L. Qiao, A.A. Volinsky, Pitting initiation and propagation of X70 pipeline steel exposed to chloride containing environments, Materials 10 (2017) 1–14, https://doi.org/10.3390/ma10091076.

[34] M. Itagaki, A. Matsuzaki, K. Watanabe, The electrochemical impedance response of transpassive dissolution of chromium in neutral solutions containing sodium chloride and sodium fluoride, Corros. Sci. 37 (1995) 1867-1878, https://doi.org/10.1016/0010-938X(95)00092-X.

[35] M. Bojinov, I. Betova, G. Fabricius, T. Laitinen, R. Raicheff, T. Saario, The stability of the passive state of iron–chromium alloys in sulphuric acid solution, Corros. Sci. 41 (1999) 1557-1584, https://doi.org/10.1016/S0010-938X(99)00003-7.

[36] I. Betova, M. Bojinov, T. Laitinen, K. Mäkelä, P. Pohjanne, T. Saario, The transpassive dissolution mechanism of highly alloyed stainless steels: I. Experimental results and modelling procedure, Corros. Sci. 44 (2002) 2675-2697, https://doi.org/10.1016/S0010-938X(02)00073-2.

[37] I. Betova, M. Bojinov, T. Laitinen, K. Mäkelä, P. Pohjanne, T. Saario, The transpassive dissolution mechanism of highly alloyed stainless steels: II. Effect of pH and solution anion on the kinetics, Corros. Sci. 44 (2002) 2699-2723, https://doi.org/10.1016/S0010-938X(02)00074-4.

[38] C.A. Huang, Y.Z. Chang, S.C. Chen, The electrochemical behavior of austenitic stainless steel with different degrees of sensitization in the transpassive potential region in 1 M H_2SO_4 containing chloride, Corros. Sci. 46 (2004) 1501-1513, https://doi.org/10.1016/j.corsci.2003.09.020.

[39] I. Betova, M. Bojinov, T. Tzvetkof, Transpassive dissolution mechanism of ferrous alloys in phosphoric acid/acetic acid mixtures, J. Solid State Electrochem. 9 (2005) 154–167, https://doi.org/10.1007/s10008-004-0566-1.

[40] M.A. Domínguez-Aguilar, R.C. Newman, Detection of deleterious phases in duplex stainless steel by weak galvanostatic polarization in alkaline solution, Corros. Sci. 48 (2006) 2560-2576, https://doi.org/10.1016/j.corsci.2005.08.017.

[41] K. Shiobara, Y. Sawada, S. Morioka, Potentiostatic study on the anodic behavior of iron-chromium alloys, Trans. Japan Inst. of Metals, 6 (1965) 58-62, https://doi.org/10.2320/matertrans1960.6.58.

Table caption

Table 1. Chemical composition (wt.%) of the different phases determined by FE-SEM/EDS (SZ = segregated zone). PREN = Cr + 3.3 3 Mo.

Table 2. Chemical composition (wt.%) of the different phases visible in Fig. 2 determined by FE-TEM/EDS.

Table 3. Chemical composition (wt.%) of the different phases visible in Fig. 5(c) determined by FE-SEM/EDS.

Figure caption

Fig. 1. (a-b) Cross-sectional FE-SEM images after mechanical polishing of the microstructure of UNS S32750 SDSS derived from conventional casting processes within a region located close to the middle of the plate. The circles in (a) represent the microcapillary diameter.

Fig. 2. (a) FE-TEM image of a precipitate (numbers represent the locations of FE-SEM/EDS point analyses). (b-d) Experimental selected area diffraction patterns obtained in different sites located by circles in (a).

Fig. 3. Profiles of Cr, Mn, Fe, Ni and Mo (FE-TEM/EDS, spatial resolution of 1.3 nm) across (a) ferrite and (b) austenite / sigma interfaces.

Fig. 4. (a) Global and local polarisation curves (1 mV/s) of different sites in 3M NaCl, pH=1, at 80 °C. FE-SEM images of (b-c) large pits far from the SZ and (d) sigma phase in the segregated zone (SZ). (e) Optical image after local polarisation curve in the segregated zone containing the sigma phase.

Fig. 5. (a-b) FE-SEM images of the segregated zone with sigma, austenite and ferrite after interrupting the global polarisation curve at a potential of -0.2 V vs SCE (γ = austenite, α = ferrite, σ = sigma). (c) AFM profile along ferrite grain / sigma particle / austenite grain.

Fig. 6. (a-c) FE-SEM images of sigma and secondary austenite after interrupting the global polarisation curve at a potential of -0.2 V vs SCE (γ = austenite, γ_2 = secondary austenite, α = ferrite, σ = sigma). (d) AFM profile through secondary austenite.

Fig. 7. (a-e) FE-SEM micrographs of sites containing sigma after PPT performed with different values of the applied potential and number of cycles.

Fig. 8. (a) AFM image of a site containing sigma phase + γ_2 after PPT test (E_a = 1 V vs SCE, N = 20 cycles) and (b) profiles along the solid line visible in (a).

		Si	Cr	Mn	Fe	Ni	Mo	PREN
Inside the SZ	sigma	0.6±0.1	29.6±0.3	1.2±0.1	55.1.2±1.1	5.8±0.3	7.8±0.7	
	austenite	0.5±0.1	26.5±0.3	1.3±0.2	57.5±0.4	9.8±0.3	4.4±0.1	41
	ferrite	0.6±0.1	28.8±0.4	1.1±0.1	56.1±0.2	6.3±0.3	7.1±0.2	52.2
Outside the SZ	austenite	0.4±0.1	25.8±0.2	1.0±0.1	61.2±0.4	8.5±0.1	3.2±0.1	36.4
	ferrite	0.5±0.1	27.8±0.2	0.9±0.1	59.9±0.1	5.7±0.2	5.2±0.1	45

Table 1. Chemical composition (wt.%) of the different phases determined by FE-SEM/EDS (SZ = segregated zone). PREN = Cr + 3.3 3 Mo.

	Cr	Mn	Fe	Ni	Mo
Point #1 (ferrite)	31.1	0.8	59.6	5.4	3.1
Point #2 (sigma)	32.4	0.9	54.2	6.0	6.6
Point #3 (austenite)	27.5	1	57.9	10.5	3.2

Table 2. Chemical composition (wt.%) of the different phases visible in Fig. 2 determined by FE-TEM/EDS.

	Si	Cr	Fe	Ni	Mo
Point #1 (sigma)	0.4	28.3	57.4	7.1	6.6
Point #2 (sigma)	0.4	28.4	56.6	7.6	6.6
Point #3 (sigma)	0.3	27.7	57.6	7.6	6.4
Point #4 (secondary austenite)	0.3	22.9	66.6	7.5	2.2
Point #5 (secondary austenite)	0.4	21.5	66.4	9	1.6
Point #6 (ferrite)	0.4	28.8	57.7	7	5.8
Point #7 (austenite)	0.3	24.4	59.8	11.7	3.3
Point #8 (austenite)	0.3	24.7	59.1	11.7	3.8
Point #9 (austenite)	0.3	25.3	59	12	3

Table 3. Chemical composition (wt.%) of the different phases visible in Fig. 5(c) determined by FE-SEM/EDS.

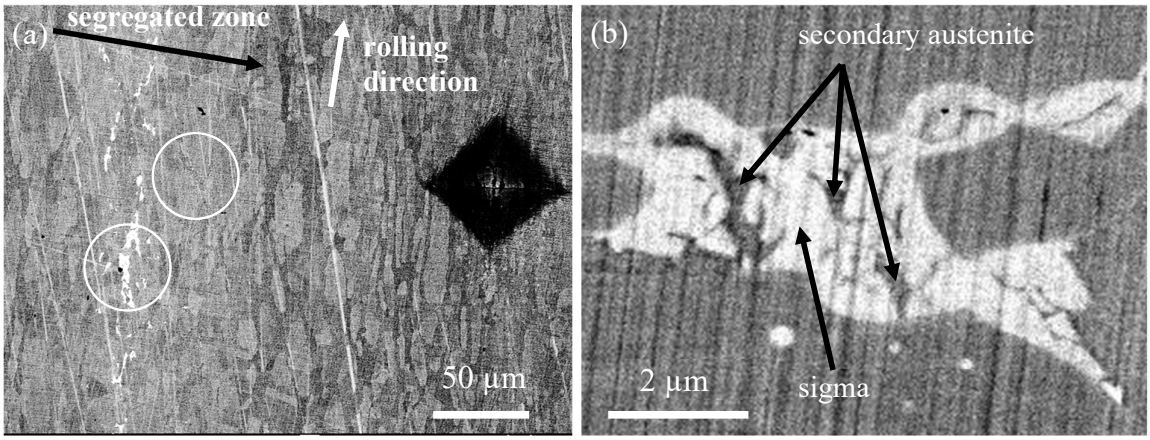

Fig. 1. (a-b) Cross-sectional FE-SEM images after mechanical polishing of the microstructure of UNS S32750 SDSS derived from conventional casting processes within a region located close to the middle of the plate. The circles in (a) represent the microcapillary diameter.

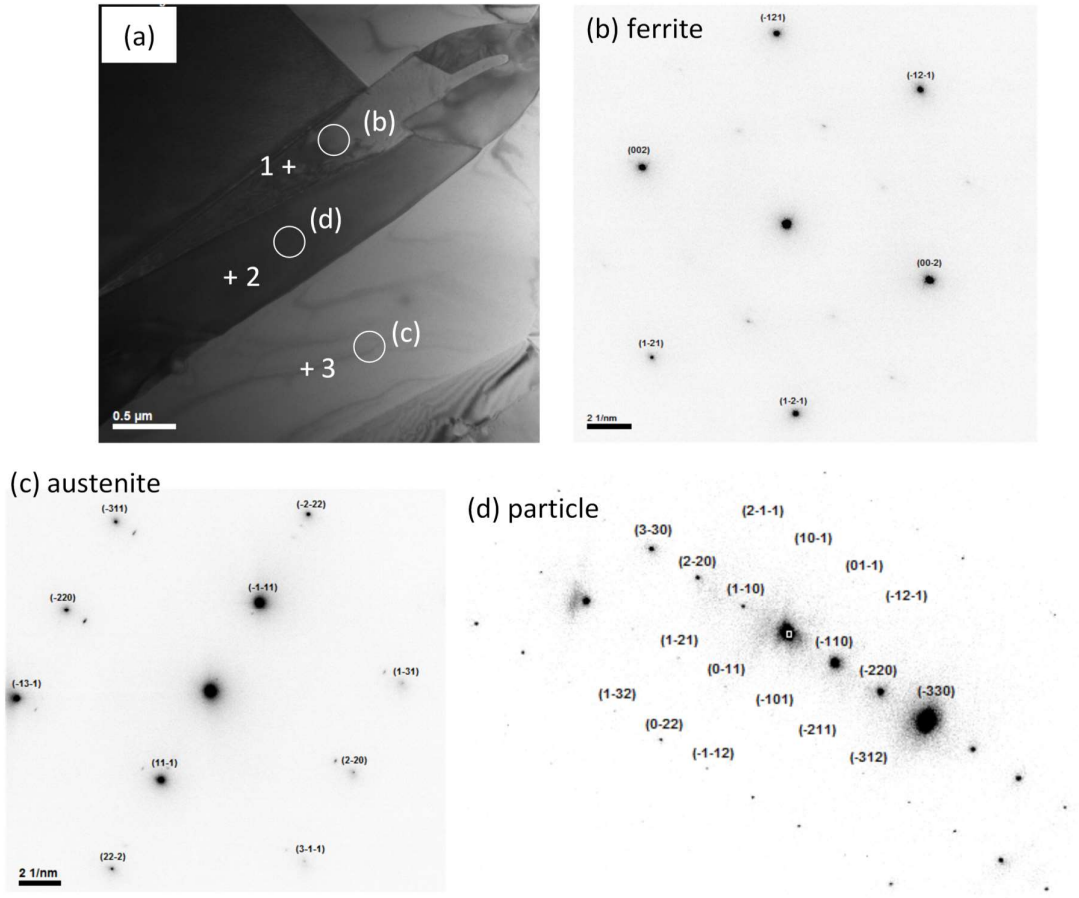

Fig. 2. (a) FE-TEM image of a precipitate (numbers represent the locations of FE-SEM/EDS point analyses). (b-d) Experimental selected area diffraction patterns obtained in different sites located by circles in (a).

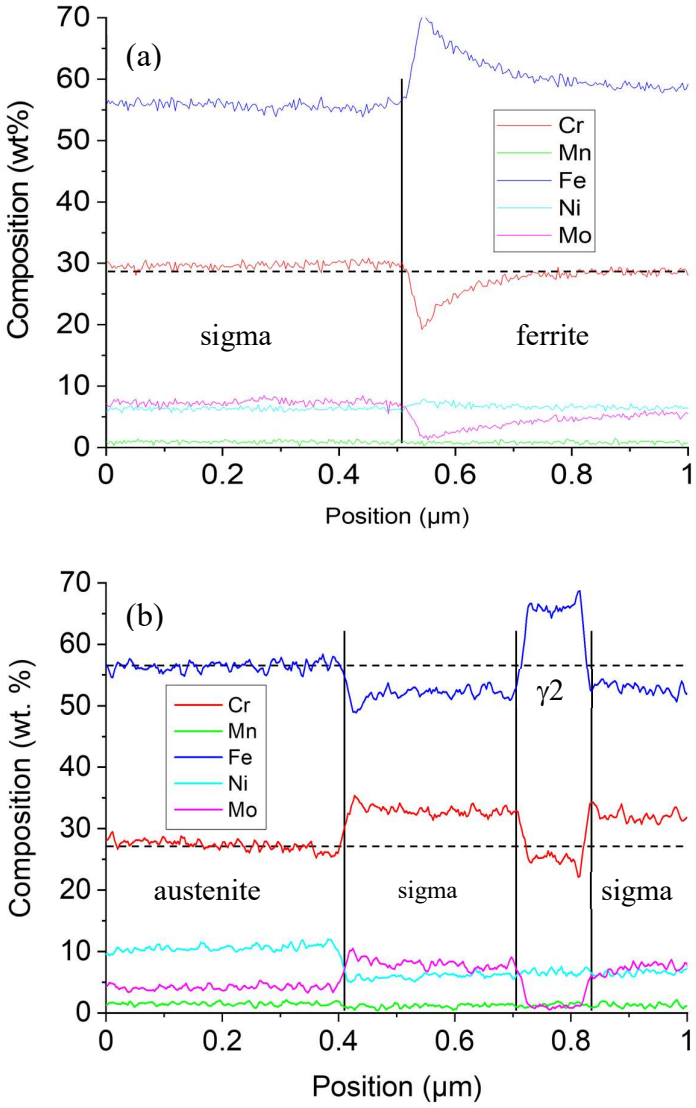

Fig. 3. Profiles of Cr, Mn, Fe, Ni and Mo (FE-TEM/EDS, spatial resolution of 1.3 nm) across (a) ferrite and (b) austenite / sigma interfaces.

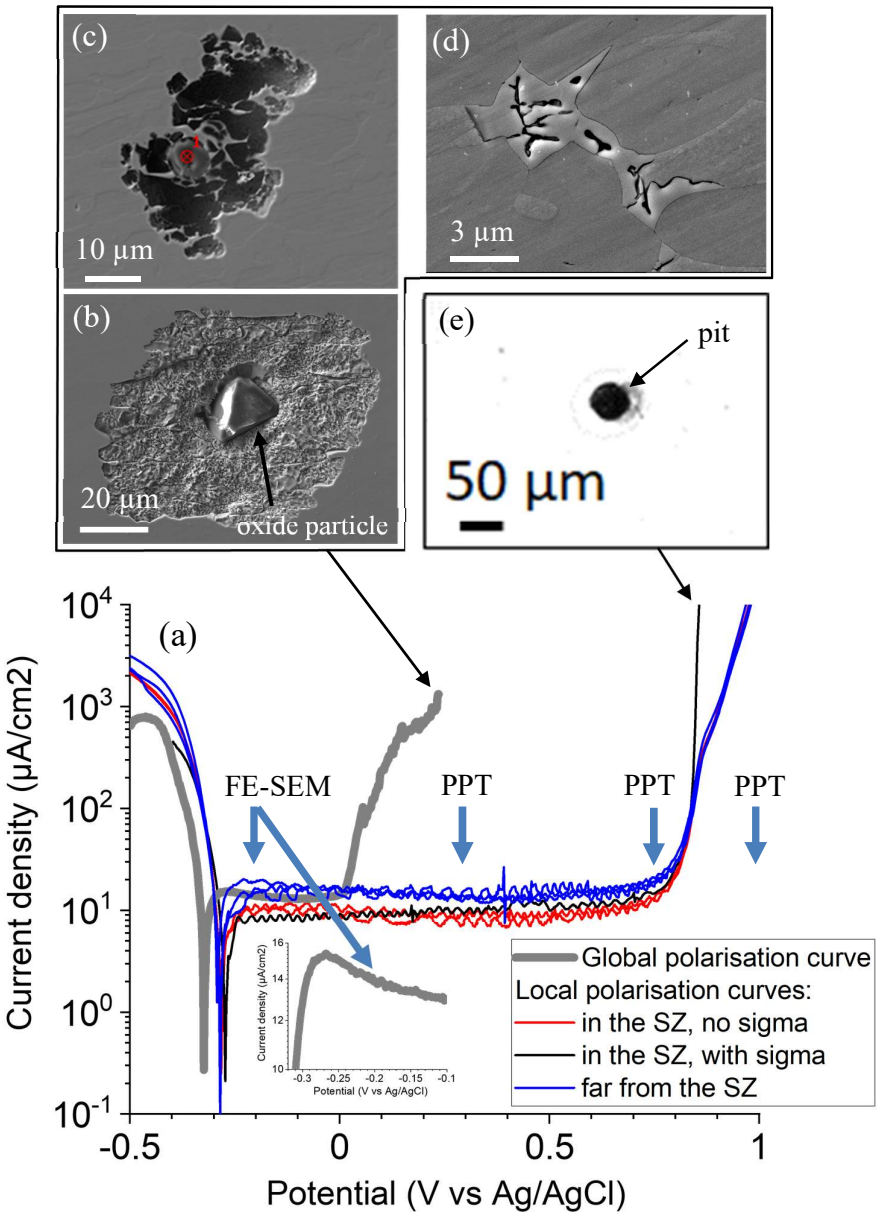

Fig. 4. (a) Global and local polarisation curves (1 mV/s) of different sites in 3M NaCl, pH=1, at 80 °C. FE-SEM images of (b-c) large pits far from the SZ and (d) sigma phase in the segregated zone (SZ). (e) Optical image after local polarisation curve in the segregated zone containing the sigma phase.

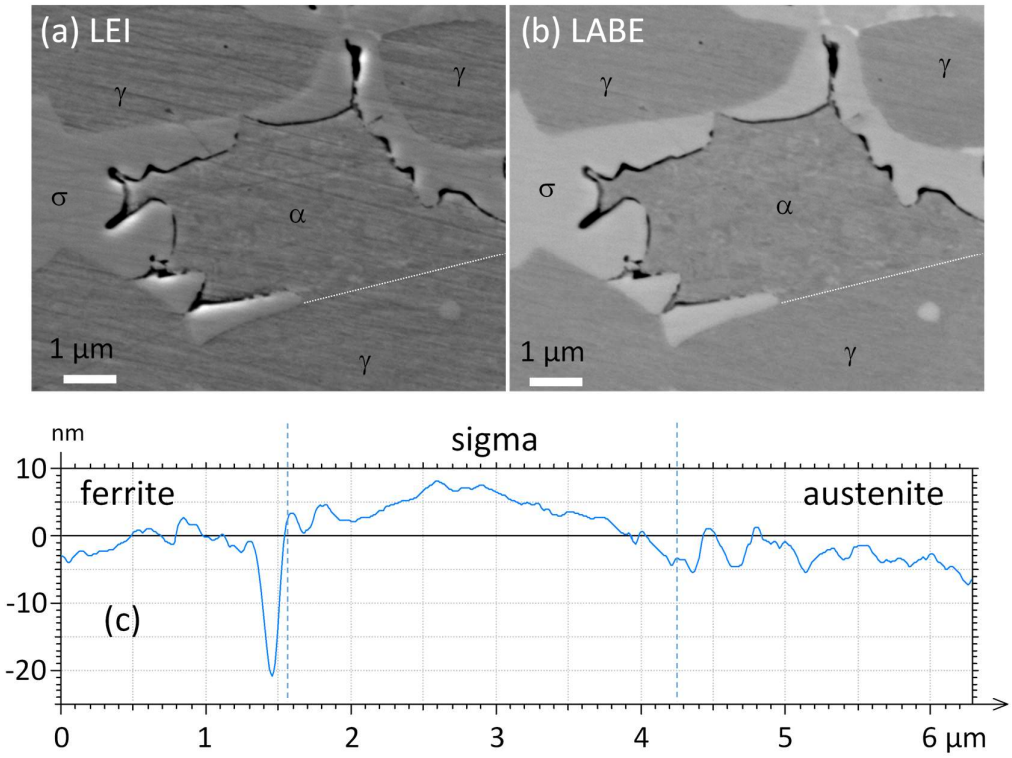

Fig. 5. (a-b) FE-SEM images of the segregated zone with sigma, austenite and ferrite after interrupting the global polarisation curve at a potential of -0.2 V vs SCE (γ = austenite, α = ferrite, σ = sigma). (c) AFM profile along ferrite grain / sigma particle / austenite grain.

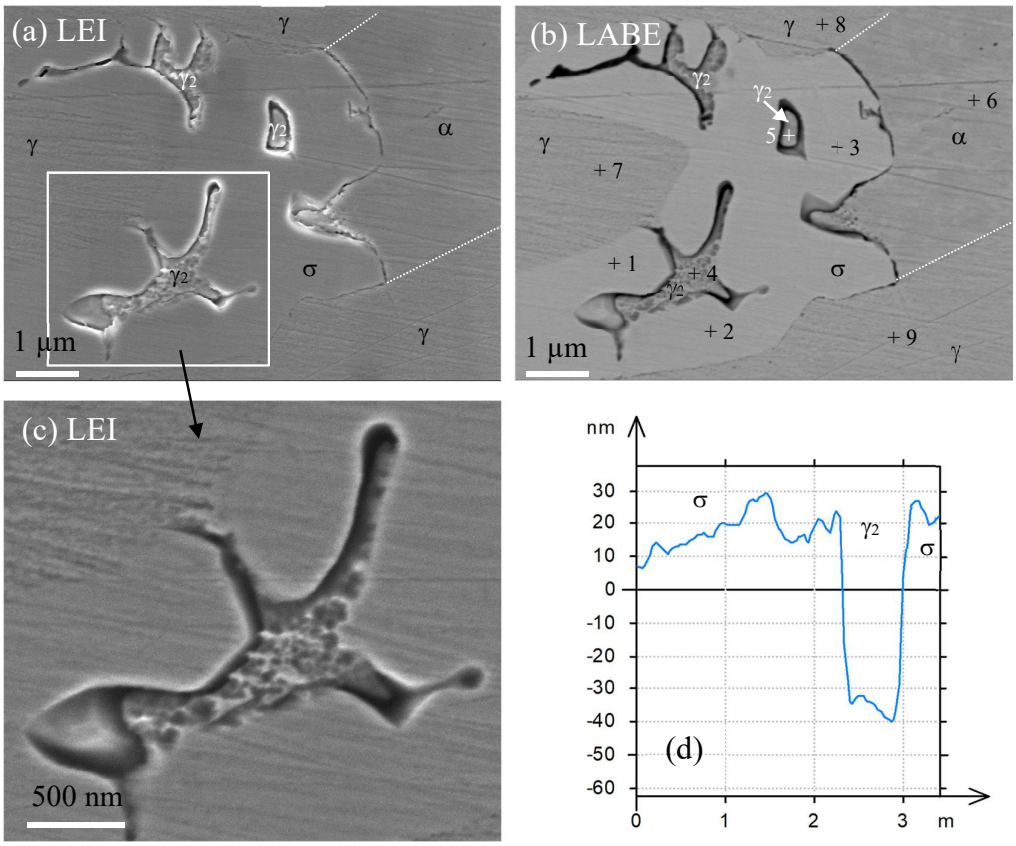

Fig. 6. (a-c) FE-SEM images of sigma and secondary austenite after interrupting the global polarisation curve at a potential of -0.2 V vs SCE (γ = austenite, γ_2 = secondary austenite, α = ferrite, σ = sigma). (d) AFM profile through secondary austenite.

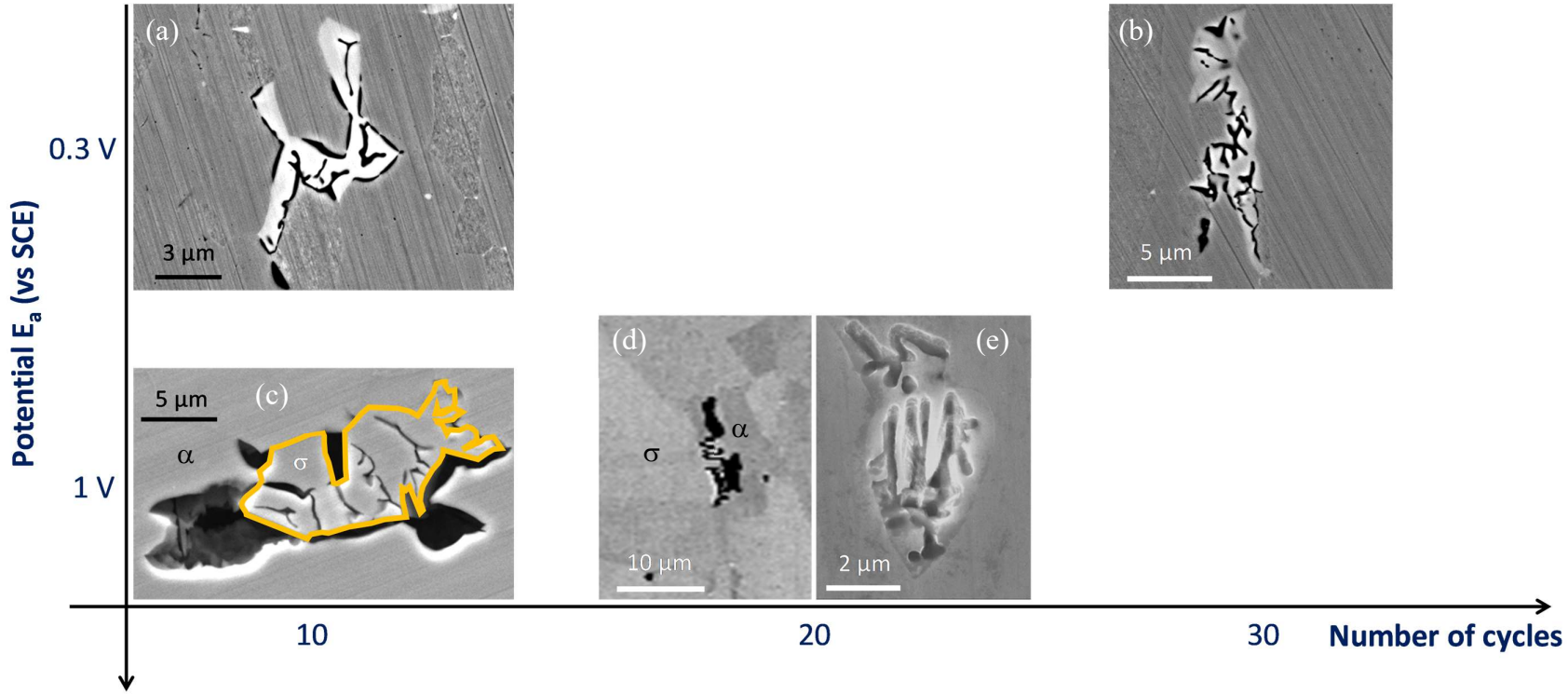

Fig. 7. (a-e) FE-SEM micrographs of sites containing sigma after PPT performed with different values of the applied potential and number of cycles.

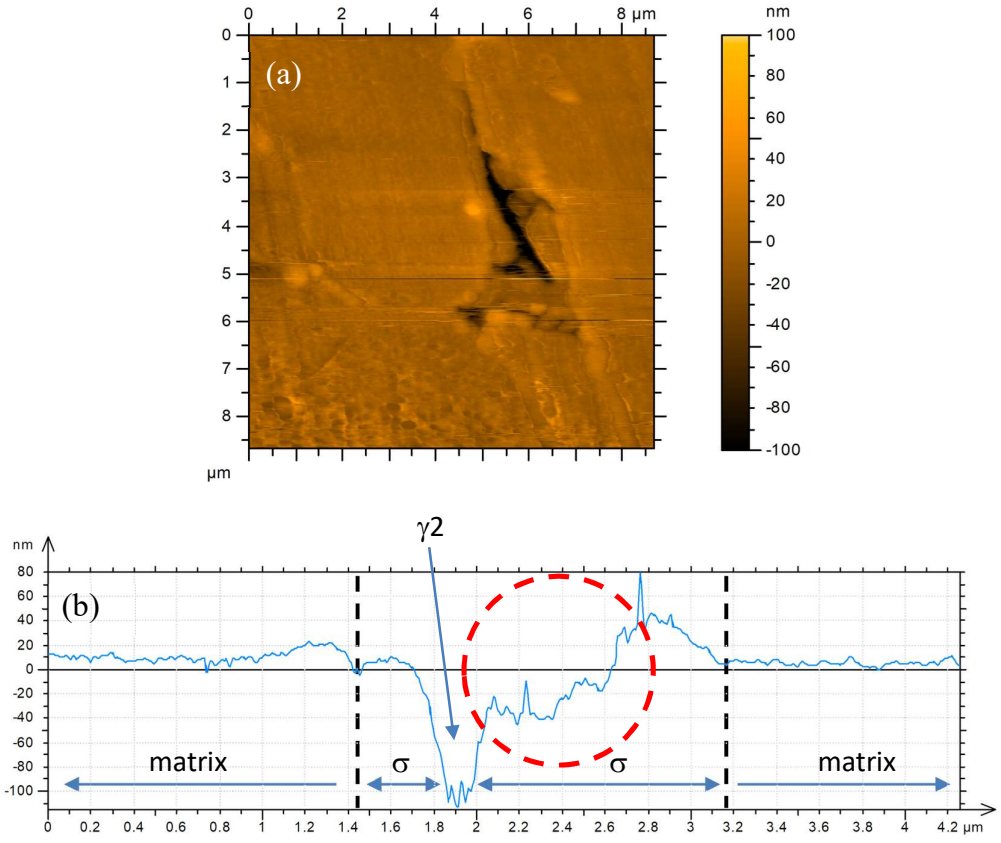

Fig. 8. (a) AFM image of a site containing sigma phase + γ_2 after PPT test (E_a = 1 V vs SCE, N = 20 cycles) and (b) profiles along the solid line visible in (a).